



Budgets of Turbulent Kinetic Energy and Reynolds Normal Stresses in Coaxial Jets with and Without Swirl: A Numerical Study

Pravin Ananta Kadu^{a,*}, Yasuhiko Sakai^b, Yasumasa Ito^b, Koji Iwano^b, Masatoshi Sugino^b, Takahiro Katagiri^c, Toshiyuki Hayase^d, Koji Nagata^e

^aDepartment of Mechanical Science & Engineering, Nagoya University, Nagoya 464-8603, Japan.

^bDepartment of Mechanical Systems Engineering, Nagoya University, Nagoya 464-8603, Japan.

^cInformation Technology Center, Nagoya University, Nagoya 464-8601, Japan.

^dInstitute of Fluid Science, Tohoku University, Sendai 980-8577, Japan.

^eDepartment of Aerospace Engineering, Nagoya University, Nagoya 464-8603, Japan

ARTICLE INFO

Received : 20 June 2019
Revised : 28 August 2019
Accepted : 04 October 2019

Keywords:

Jets, Swirl, turbulent kinetic energy budget, Reynolds normal stress budget, Numerical simulation

ABSTRACT

The influence of swirl on the budgets of turbulent kinetic energy and Reynolds normal stresses is investigated for the configuration of coaxial jets by using direct numerical simulation (DNS) method. A case of strong swirl is studied and compared with a non-swirling case. As the consequence of strong swirl, a vortex breakdown bubble (VBB) is formed. Budget analysis of turbulent kinetic energy (TKE) shows that the higher energy produced at shear layers of upstream region of central stagnation point as the consequence of swirl is transported to the outer jet central region through turbulent diffusion. Moreover, TKE in outside region of VBB is convected from highly energetic upstream region to the downstream region in swirling case, whereas the positive contribution by convection term in non-swirling case seems to be smaller. Budget analysis of the Reynolds normal stresses in upstream region of central stagnation point uncovers that the pressure-strain correlation term acts as energy sink for radial component of Reynolds normal stress at outer shear layer in the swirling case contrary to non-swirling case. In swirling case, a distinctive negative production of the radial component of Reynolds normal stress is observed upstream of central stagnation point in the inner shear layer.

© 2020 ISEES, All rights reserved

1. Introduction

The industrial applicability of swirling jets ranges from the burners to heat exchangers. An ideal industrial burner, in particular, needs the abilities of efficient mixing of fuel with the oxidant, preventing combustion flame from blowing out and reusing heated products of combustion to improve efficiency. Swirling jets fulfill these characteristics and therefore it captures the attention of numerous researchers.

The detailed study of coaxial jets without swirl is performed by, for example, Buresti et al. [1998], Rehab et al. [1997], and Abboud and Smith [2014]. Their findings suggest that the length of the inner potential core can be adjusted by the ratios of inner to outer jets velocity and diameter. But for the velocity ratio around 0.5, the potential core is still extended over a considerable axial distance delaying the mixing.

The other mean of altering the potential core length is by introducing the swirl in the jet. The experimental investigation of the effect of mild swirl in coaxial jets is carried by Ribeiro and Whitelaw [1980]. They illustrated that in the presence of the swirl, a radial static pressure gradient is set up as it is proportional to the mean squared azimuthal velocity divided by the radial distance. The fact of decay in azimuthal velocity in the downstream region creates an adverse pressure gradient in the axial direction. The outcome of this process is the decay of centerline streamwise velocity, the increased rate of spread of the jet and ultimately the mixing

enhancement. Moreover, if the swirl number (the ratio of the axial flux of momentum in the azimuthal direction to that in the axial direction) exceeds a certain threshold value, the internal recirculation zone, a property of the vortex breakdown, appears [Ben-Yeoshua, 1993; Champagne and Kromat, 2000]. The swirl number and the ratio of mass flow rates of two jets also dictate the type of vortex breakdown. The distinct types of vortex breakdown [Sarpkaya, 1971; Lucca-Negro and O'doherty, 2001; Billant et al., 1998] identified are namely, (a) double helix, (b) spiral, (c) axisymmetric bubble, and (d) conical.

Another striking effect of the swirl is the surge in Reynolds stresses. Mehta et al. [1991] demonstrated this experimentally for the single swirl jet configuration. It was shown that the introduction of swirl elevates all the six independent components of Reynolds stresses. The increase in the radial spread of the Reynolds stresses was also observed indicating the growth of the mixing layer. Similar observations were also made by Ribeiro and Whitelaw [1980] for the configuration of coaxial jets. This feature of increment in the Reynolds stresses along with their spread is vital for the mixing enhancement. However, the reasons for the surge in Reynolds stresses and hence the turbulent kinetic energy in coaxial swirling jets have not been thoroughly explored yet. Therefore, in the present study, an attempt is made to examine this with the help of the budgets of Reynolds stresses and turbulent kinetic energy.

* Corresponding Author: : kadu.pravin.ananta@h.mbox.nagoya-u.ac.jp

In the present study, a configuration of unconfined coaxial jets with a strong swirl is investigated and compared with a case of non-swirl. Computational fluid dynamics (CFD) have been used extensively in the past [Dinesh et al., 2010; Javadi and Nilsson, 2015; Balaji et al., 2016] to acquire in-depth knowledge of the swirling flows and is also used in the present study. The numerical results are validated with the experimental measurements. In §2, the numerical details are explained. Development of mean flow variables is presented in §3.1. The results of Reynolds stresses and turbulent kinetic energy are explained in §3.2. Budget analysis is presented for the turbulent kinetic energy and Reynolds normal stresses in §3.3. Based on the results obtained in regards to the various effects of swirl on coaxial jets, the conclusion is made in §4.

2. Numerical Method

2.1. Governing equations

The three-dimensional, incompressible, unsteady Navier-Stokes equations are solved on the structured-Cartesian grid for the viscous Newtonian fluid motion along with the continuity equation. The non-dimensional form of Navier-Stokes equations and continuity equation are as follows:

$$\frac{\partial u_i}{\partial t} + u_j \frac{\partial u_i}{\partial x_j} = -\frac{\partial p}{\partial x_i} + \frac{1}{Re_D} \frac{\partial^2 u_i}{\partial x_j \partial x_j} \tag{1}$$

$$\frac{\partial u_i}{\partial x_i} = 0 \tag{2}$$

Here, Re_D is the Reynolds number defined as $Re_D = U_{ij} D / \nu$, where U_{ij} and D are the inner jet bulk velocity and diameter respectively, and ν the kinematic viscosity.

2.2. Computational domain and numerical discretization

Fig. 1(a) shows the schematic of the nozzle exit configuration and the computational domain. The nozzle axis coincides with the x -axis, i.e., streamwise direction, while y and z axes originate from the nozzle axis. The dimensions of the nozzle exit are expressed in terms of the inner jet diameter D . The DNS computational domain size $L_x \times L_y \times L_z$ is taken as larger ($20D \times 28D \times 28D$) for swirling case as opposed to the non-swirling case ($20D \times 20D \times 20D$) due to the expected higher growth rate in swirling case.

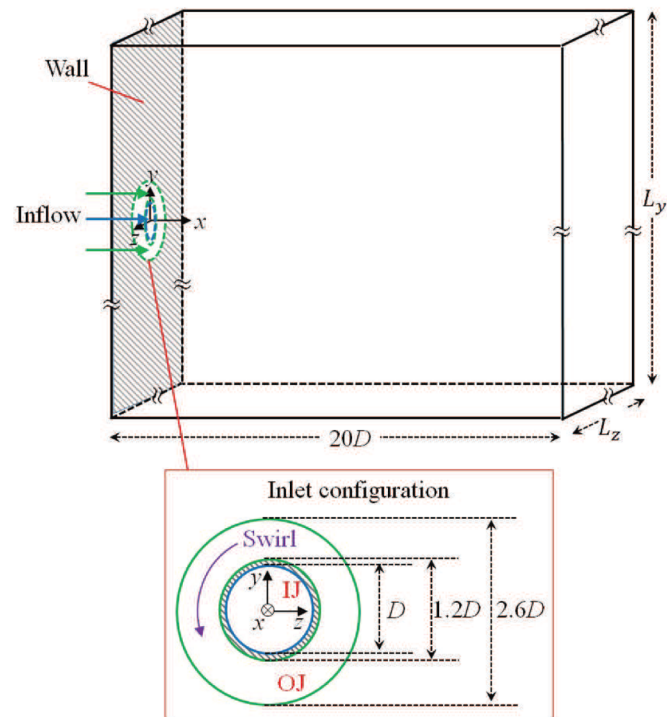


Fig. 1(a) Schematic of the nozzle exit configuration and computational domain. Here, IJ is the inner jet and OJ is the outer jet. Note that the inner jet pipe has a thickness of 0.1D.

The fractional step method [Kim and Moin, 1985] is employed to solve the governing equations, resulting in the Poisson equation for pressure in place of the continuity equation. Conjugate gradient method [Nocedal and Wright, 2006] is used to solve the Poisson equation. The second-order Runge-Kutta method is used for the time integration. The grid is staggered and equally-spaced. The conservative scheme of Morinishi et al. [1998] is employed for the convection term and central difference scheme is used for the viscous term. The spatial discretization is fourth-order accurate in x direction, while it is second-order accurate in y and z directions.

2.3. Boundary conditions

2.3.1. Inflow boundary condition

A challenge in investigating the swirling flow is the implementation of inlet boundary condition for the computational domain. The swirling flow can be generated by various methods, such as using the guiding vanes, rotating pipe, and tangential injection. These methods affect the distribution of mean velocity components and hence can alter the vortex behavior [Lucca-Negro and O'doherty, 2001]. Apart from the mean velocity, the correlations between the instantaneous velocity components are also vital [Abboud and Smith, 2014]. Therefore, an attempt is made to improve the inflow boundary condition by using precursor simulations of jet nozzles in advance of the DNS simulations. The procedure involves the generation of a library of instantaneous velocity components at the nozzle exits and mapping it onto the inlet fictitious cells of DNS grid by using interpolation.

Fig. 1(b) depicts the outer jet nozzle configuration. The swirl is generated using four guiding vanes which are tilted by an angle α . The four inlets with diameter D are placed equidistant at the edge of outer casing. The 10.6D long outer jet pipe has the inner diameter 1.2D and the outer diameter 2.6D. The cell count of outer jet nozzle is around 4.39 million and the cells are of prism type. Fig. 1(c) depicts the inner jet nozzle of exit diameter D and length 24D. An annular pipe of length 5.5D is used at the upstream to generate the turbulence. The cell count of inner jet nozzle is 3.13 million and the cells are also of prism type.

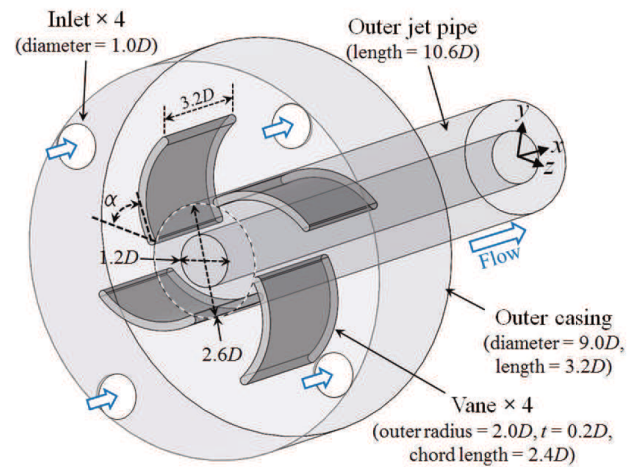


Fig. 1(b) Outer jet (OJ) nozzle configuration.

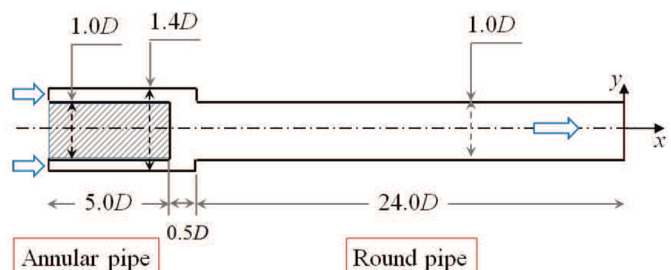


Fig. 1(c) Inner jet (IJ) nozzle configuration: cross-sectional view.

The vanes are oriented by $\alpha = 90^\circ$ to generate the strong swirl, while they are removed for the case of non-swirling case. These simulations for nozzles are run in Open FOAM and large eddy simulation (LES) with the dynamic Smagorinsky model is used here due to the limitation of the computational resources. The second order implicit scheme is used for the time derivative and second order Gaussian scheme is used for the spatial discretization. The solver used is the *pimpleFoam* which is based on the PIMPLE (merged PISO-SIMPLE: pressure implicit with splitting of operator and semi-implicit method for pressure-linked equations) algorithm. The Reynolds number for inner pipe (Re_p) is 2200. The flow rate ratio between outer to inner jet (Q_{o}/Q_i) in both the cases is 10.64 and the resulting bulk velocity ratio (Q_{o}/Q_i) is 2.0. The flow rates through the four inlets of outer jet nozzle and upstream annular pipe of inner jet nozzle are adjusted accordingly.

Fig. 1(d) shows the profiles of the mean streamwise velocity (\bar{U}) and mean azimuthal velocity (\bar{V}_θ) just at the exit of nozzle. The turbulent profile of mean streamwise velocity is obtained for the inner jet. The effect of introduction of vanes can be seen on the mean streamwise velocity for the outer jet. Moreover, a significant higher mean azimuthal velocity is recorded for the swirling case. To account the swirling strength, the swirl number Sw [Ribeiro and Whitelaw, 1980; Champagne and Kromat, 2000] is used, which is the ratio of the axial flux of momentum in the azimuthal direction to that in the axial direction,

$$Sw = \frac{\int_0^{R_0} \bar{U} \bar{V}_\theta r^2 dr}{R_0 \int_0^{R_0} (\bar{U}^2 - \bar{V}_\theta^2 / 2) r dr} \quad (3)$$

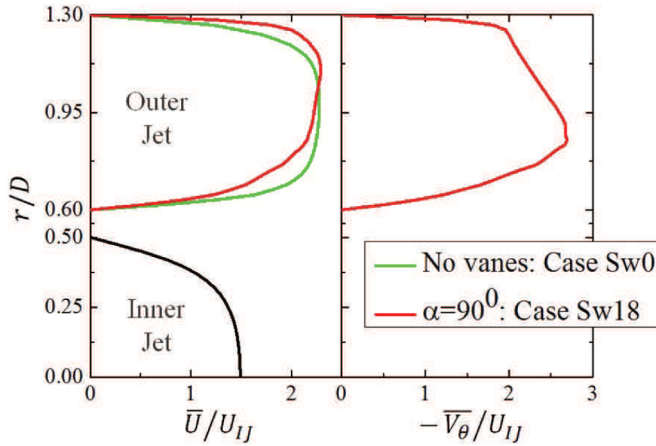


Fig. 1(d) Radial distribution of the mean velocity components at the nozzle exit.

Here, R_0 is the outer radius of outer jet. The swirl number, calculated by using above formulation and mean velocity profiles, is 1.8 for the swirling case and 0 for the non-swirling case. These cases are named respectively as case Sw18 and case Sw0 throughout this text. The nozzle exit streamwise ($\sqrt{u'^2}/U_{IJ}$), azimuthal ($\sqrt{v_\theta'^2}/U_{IJ}$), and radial ($\sqrt{v_r'^2}/U_{IJ}$)

turbulence intensities are reported in Fig. 1(e). Inner jet exhibits the typical distribution of velocity fluctuations as seen for the internal flow. The turbulence level in the outer jet is observed to be higher as compared to the inner jet. Furthermore, these fluctuations are increased considerably with the introduction of swirl.

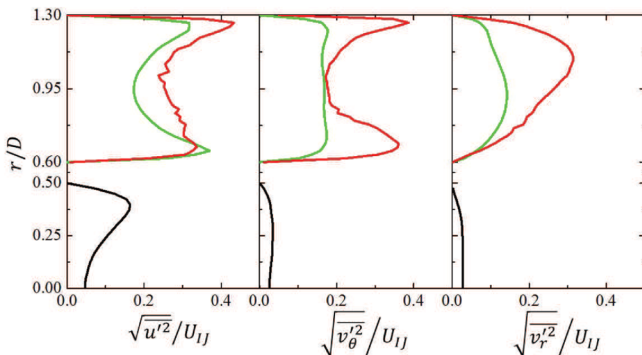


Fig. 1(e) Radial distribution of the turbulence intensities at the nozzle exit.

2.3.2. Cross-stream and outflow boundary conditions

The cross-stream boundaries are employed with the Neumann boundary condition, $\partial\Theta/\partial n=0$, where Θ refers to the velocity components. The convective outflow boundary condition [Miyachi et al., 1996] is used for the outlet plane:

$$\frac{\partial u_i}{\partial t} + U_c \frac{\partial u_i}{\partial x} = \frac{1}{Re_D} \frac{\partial^2 u_i}{\partial x_j \partial x_j} \quad (4)$$

where U_c is the convective velocity and is computed over the circular strips by formula,

$$U_c = \frac{\sum(u_p \cdot A_p)}{\sum A_p} \quad (5)$$

Here, u_i is the instantaneous streamwise velocity of the cell and A_i is the area of same cell. The numerator in the formulation computes the flow rate through the circular strip, while the denominator is the area of strip. The technique is implemented to account for the radial change in streamwise velocity.

2.4. Simulation details

The grid size ($N_x \times N_y \times N_z$) is $700 \times 700 \times 700$ for case Sw0 and $700 \times 980 \times 980$ for case Sw18. The grid resolution $\Delta = (\Delta_x \Delta_y \Delta_z)^{1/3}$ is of the order of the Kolmogorov length scale η . The maximum Δ/η is located at the outer shear layer of the cross section $x = 1.0D$ in both cases and is equal to 5.1 and 7.1 for cases Sw0 and Sw18, respectively. The CFL number is kept around 0.3. The simulations are run for 324 and 230.4 time scales D/U_{IJ} for the cases Sw0 and Sw18 respectively before initiating the extraction of statistical data. Then the statistical data (i.e. Reynolds time-averaged data) are evaluated from the instantaneous data of 1296 and 1056 time scales D/U_{IJ} for the cases Sw0 and Sw18 respectively, which are observed to be enough to get statistically steady results for the mean velocity components and Reynolds stresses. Note that the time-steps for cases Sw0 and Sw18 are $0.00405 D/U_{IJ}$ and $0.00192 D/U_{IJ}$ respectively and the instantaneous data is extracted at each time-step and each grid point. The code is written using Fortran programming language and the parallelization of code is done using the message passing interface (MPI) library. Implementation of MPI is done using the two-dimensional domain decomposition in the $y - z$ plane.

2.5. Experimental details

Experiments are performed for both the cases with the identical nozzle configuration and the flow parameters to validate the numerical results. Here, the fluid used is water, and the diameter of jet (D) and the inner jet bulk velocity (U_{IJ}) are 10 mm and 0.24 m/s respectively. The measurements of flow field are carried out by particle image velocimetry (PIV). The streamwise and radial components of velocity field are measured only. An Nd: Yag laser (DANTEC RayPower 5000) sheet of wavelength 532 nm and thickness 1 mm is used for the illumination of the test section. The seeded particles dispersed in both the jets have the mean diameter 11 μm . The flow is visualized by a high-speed video camera (Ametek Phantom V210) of 1280×800 pixel resolution. The band-pass filter (Asahi spectrometer PB0040) is affixed to the camera. The images are captured for 12 sec in $x - y$ plane with the sampling frequency of 2000 Hz. The spatial resolution to estimate the velocity field is 0.91 mm for the $x - y$ plane measurements. The captured images are converted into 8-bit digital codes. The analysis of the flow field is carried out by commercial software, DANTEC DynamicStudio.

3. Results and Discussion

3.1. Mean flow features

Fig. 2(a) shows the variation of mean streamwise velocity and mean static pressure along the centerline for both cases. In the case Sw0, the static pressure is increased in the region $x/D \leq 1.5$, which can be attributed to the slight expansion of inner jet (can be observed in the mean streamlines plot in Fig. 2(b)). Correspondingly, the streamwise velocity decreases, which is also observed in other studies [Buresti et al., 1998; Rehab et al., 1997; Abboud and Smith, 2014]. Then a negligible slope for the streamwise velocity is observed until $x/D \leq 3.0$, which also marks the end of inner jet potential core. Note that the potential core of inner jet in coaxial jets is generally the area of inner jet which is unaffected by the outer jet. Thereafter, the streamwise velocity increases due to the mixing of higher velocity outer jet with the inner jet. Increment continues until $x/D \approx 10.0$ and the decline begins afterward due to the spread. On the other hand, the

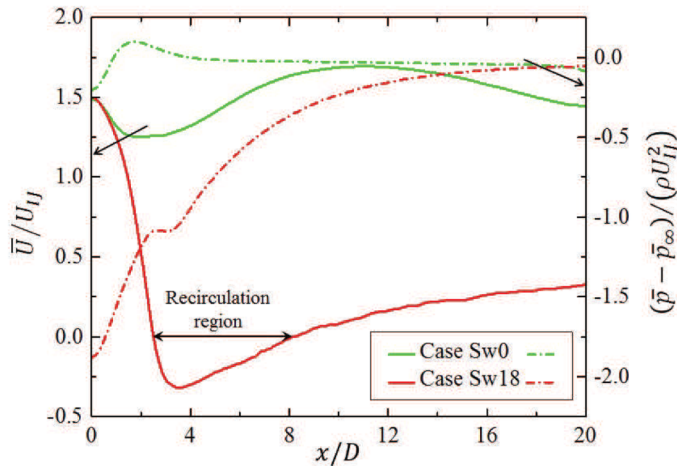


Fig. 2(a) Centerline distribution of mean streamwise velocity and mean static pressure. Solid line: mean streamwise velocity, dash-dotted line: mean static pressure.

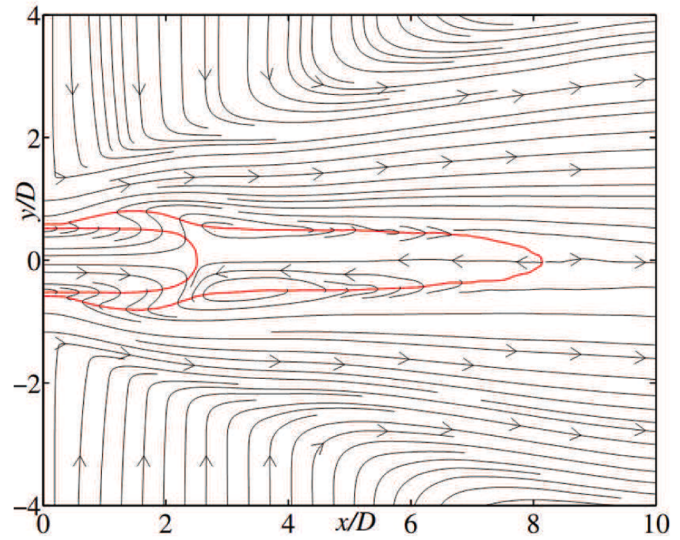


Fig. 2(c) Mean streamlines at the central x plane for case Sw18. Red line is an isoline of $\bar{U} = 0$

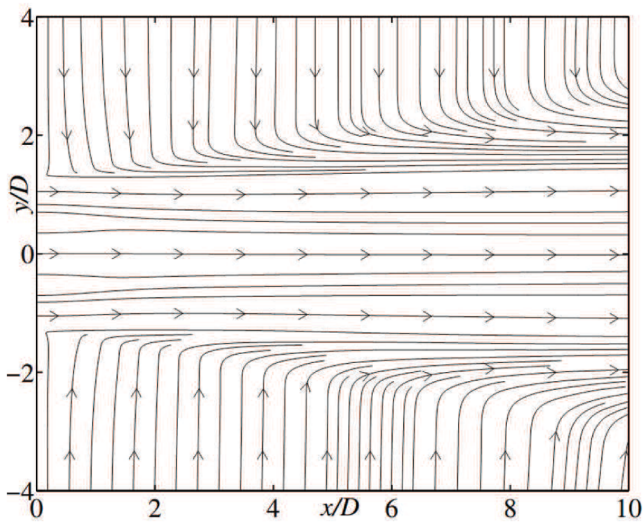


Fig. 2(b) Mean streamlines at the central x / y plane for case Sw0.

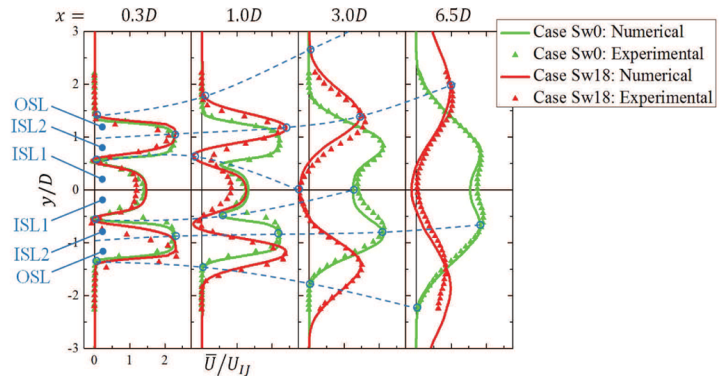


Fig. 2(d) Radial distribution of mean streamwise velocity. Dashed lines in region $y/D < 0$ enclose shear layers for case Sw0 and that in region $y/D > 0$ enclose shear layers for case Sw18.

swirling case sees the lower static pressure in the region close to the nozzle exit and can be attributed to the presence of angular momentum since it develops the positive pressure gradient in the radial direction as $\partial p / \partial r \propto \bar{V}_\theta^2 / r$ (obtained from the radial momentum equation). The fact that azimuthal velocity reduces with streamwise direction due to the expansion of jets elevates the static pressure at the centerline to reach the level of surrounding static pressure and hence the positive or adverse pressure gradient is established in the streamwise direction. The adverse pressure gradient is seen to result in the flow reversal indicating vortex breakdown. This recirculation region spans between the axial distance of $2.5D$ to $8.1D$ on the centerline. A discontinuity in the positive static pressure gradient is seen at the leading stagnation point or the vortex breakdown point on the centerline, which is consistent with the findings of Kirkpatrick [1964] and Sarpkaya [1971]. Fig. 2(c) depicts the mean streamlines and the isoline of $\bar{U} = 0$ enclosing the axisymmetric bubble type vortex breakdown or the vortex breakdown bubble (VBB). Inner jet is observed to be penetrating the bubble and hence the type is termed as the partially penetrated VBB by Santhosh et al. [2013].

Fig. 2(d) shows the radial distribution of mean streamwise velocity for both cases. In the figure, the green line and green triangle represent the case Sw0, whereas the red line and red triangle represent the case Sw18. Note that the $|y/D|$ directional distributions are referred as the radial r/D distributions due to the axisymmetric nature of the flow (this followed throughout this text). The two shear layers, inner one (termed as ISL) between the two jets and outer one (termed as OSL) in between the peak in outer jet region and surrounding ambient, are formed. Moreover, the

inner shear layer is sub-divided into ISL1 between the axis and local minima of mean streamwise velocity separating two jets, and ISL2 between local minima and peak in the outer jet region. The upstream location $x = 0.3D$ is marginally affected by the swirl. However, the faster spread of jets, the higher deceleration of IJ and the annular reversed flow between two jets (also depicted in Fig.2(c)) are observed in case Sw18 at the location $x = 1.0D$ as a contrast to the case Sw0. The stronger ISL is featured as a consequence of annular reversed flow. At $x = 3.0D$, two jets start to merge in the case Sw0, while the deceleration continues in case Sw18 to form VBB. Further downstream location $x = 6.5D$ sees the continuance of merging two jets for case Sw0, whereas the case Sw18 exhibits acceleration at the central region with the reduction of radial extent of VBB. Moreover, the higher radial outward spread of OJ is observed in swirling case as compared to the non-swirling case. The numerical results are generally found to agree well with the corresponding experimental measurements. Swirling case shows a discrepancy between numerical and experimental data at the upstream locations $x \leq 1.0D$, which can be attributed to the difficulty in obtaining the same inflow condition for numerical study as that present in the experimental investigation. However, it can be noted that the trends in both numerical and experimental data are the same.

The radial distribution of mean azimuthal velocity is depicted in Fig. 2(e) for case Sw18 and it is not presented for case Sw0 due to the absence of azimuthal momentum. The distribution shows continuous radial spread and decay with the downstream distance as expected. Its effect can be observed on the mean static pressure distribution (see Fig. 2(f)). The

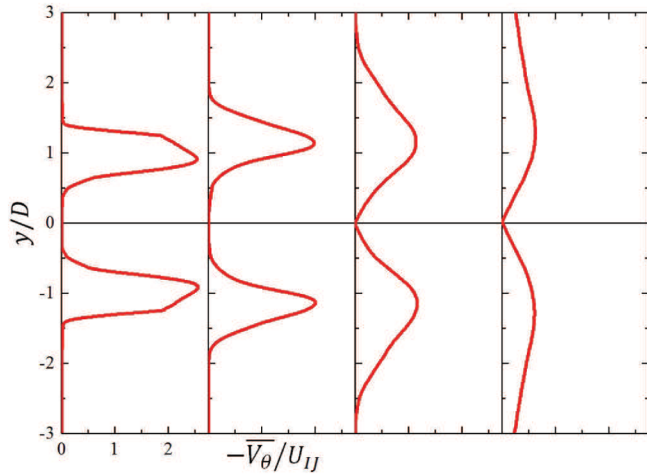


Fig. 2(e) Radial distribution of mean azimuthal velocity. Same legend as Fig. 2(d).

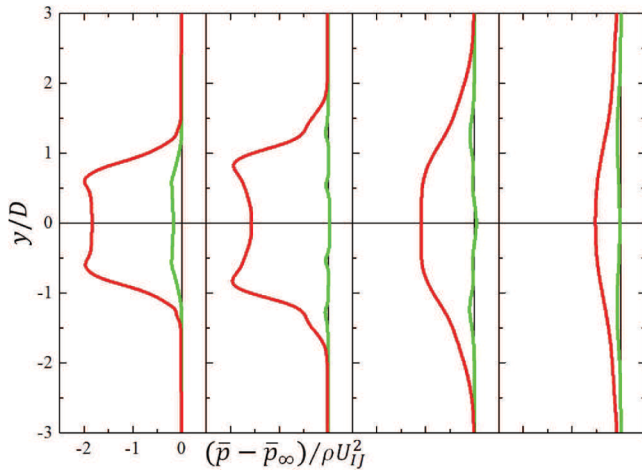


Fig. 2(f) Radial distribution of mean static pressure. Same legend as Fig. 2(d).

pressure deficit at upstream region caused by strong azimuthal momentum at the region is recovered at the downstream region as discussed earlier. The non-swirling case presents an almost flat radial profile for static pressure.

3.2. Turbulence intensities and Reynolds shear stresses

Fig. 3(a), Fig. 3(b) and Fig. 3(c) show the radial distribution of turbulence intensities (RMS of Reynolds normal stresses), and Fig. 3(d) turbulent kinetic energy at various streamwise locations. The streamwise turbulence intensity, plotted in Fig. 3(a), exhibits the same level for both the cases of Sw0 and Sw18 in the inner region $r \le 0.3D$ close to the jet exit ($x = 0.3D$), but it is higher for the case Sw18 than case Sw0 in the region $r > 0.3D$. At $x = 1.0D$, cases Sw0 exhibits a considerable increment in the level of streamwise turbulence intensity, however, the level for the swirling case is drastically increased, especially in the ISL2 ($0.6 \le r/D \le 1.2$) and OSL ($1.2 \le r/D \le 1.8$). The peaks in case Sw18 are also moved radially outward and the peak in ISL2 ($r \approx 0.9D$) exceeds the OSL peak ($r \approx 1.4D$) in magnitude. The downstream region sees the spread of streamwise turbulence intensity in radially outward as well as inward directions. The remaining turbulence intensities, i.e. azimuthal and radial turbulence intensities, are depicted in Fig. 3(b) and Fig. 3(c) respectively. Similar to streamwise turbulence intensity, the azimuthal and radial turbulence intensities also exhibit higher magnitude in case Sw18 as compared to case Sw0, especially at $x = 1.0D$. The experimental observations, presented for streamwise and radial turbulence intensities, also show a similar trend with a discrepancy in their levels.

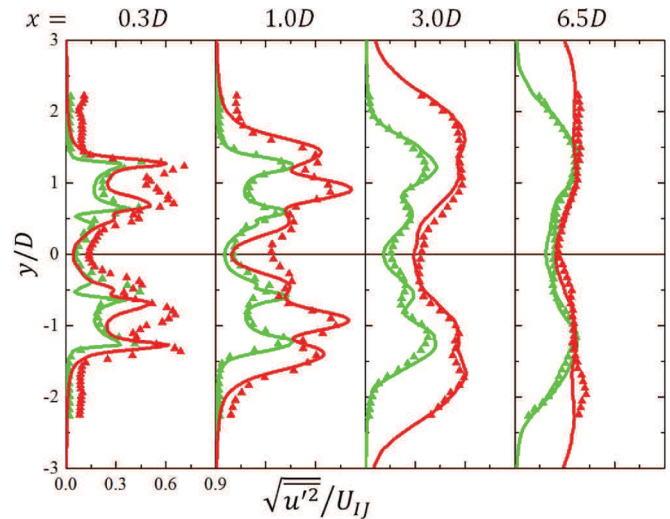


Fig. 3(a) Radial distribution of streamwise turbulence intensity. Same legend as Fig. 2(d).

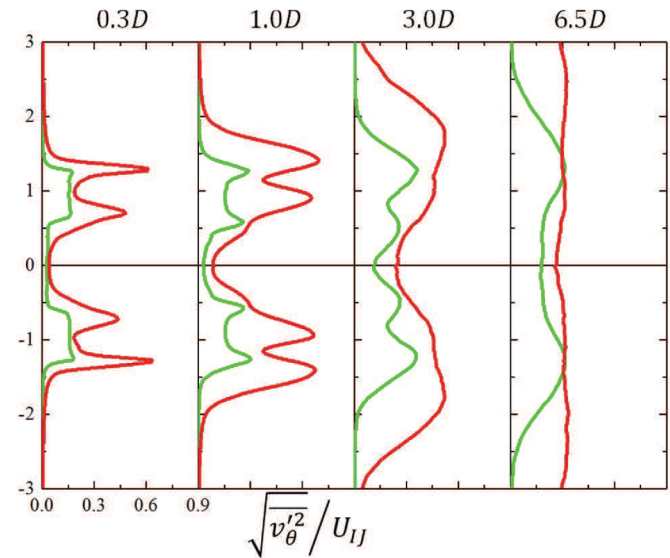


Fig. 3(b) Radial distribution of azimuthal turbulence intensity. Same legend as Fig. 2(d).

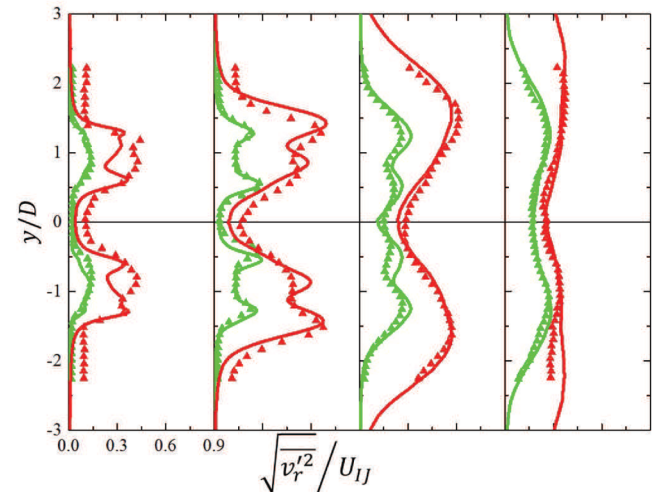


Fig. 3(c) Radial distribution of radial turbulence intensity. Same legend as Fig. 2(d).

Turbulent kinetic energy (k) in Fig. 3(d) replicates the similar trend as that in the turbulence intensities. A noteworthy intensification in the level of turbulent kinetic energy is observed at $x = 1.0D$ for swirling case as compared to the non-swirling case. The peak levels for swirling case become comparable to that for non-swirling case by $x = 6.5D$.

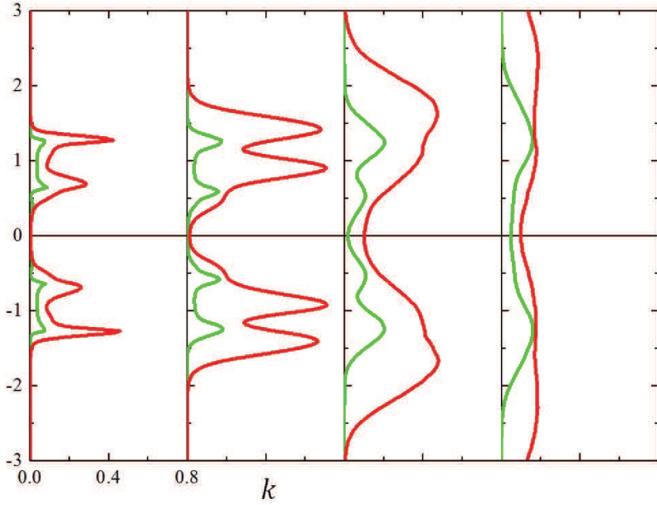


Fig. 3(d) Radial distribution of turbulent kinetic energy, $k = \overline{q^2}/2 = (\overline{u'^2} + \overline{v_\theta'^2} + \overline{v_r'^2})/2$. Same legend as Fig. 2(d).

The radial distribution of the Reynolds primary shear stress, $\overline{u'v_r'}$, is shown in Fig. 3(e). The shear stress $\overline{u'v_r'}$, which is responsible for the radial flux of axial momentum and hence for the spread of jets, is observed to be very high for case Sw18. This is the consequence of the large velocity gradients developed due to the VBB, forming the strong shear layers. The peak levels in case Sw18, however, approaches to the non-swirling case in the downstream region. The Reynolds secondary shear stresses $\overline{u'v_\theta'}$ and $\overline{v_\theta'u'}$ are plotted in Fig.3(f) and Fig. 3(g) respectively. A substantial increment for both secondary shear stress is noted in the presence of swirling motion. On the other hand, the case Sw0 does not show significant secondary shear stresses, which is due to the absence of credible azimuthal as well as radial momentum resulting into the negligible production.

The above discussion shows significant variations in the distributions of turbulent kinetic energy and Reynolds stresses due to the introduction of swirl. Thus, to examine the enhancement of turbulence level, the budgets of turbulent kinetic energy and Reynolds normal stresses are investigated for both cases at the locations $x/D = 0.3, 1.0,$ and 3.0 which see rapid changes.

3.3. Budgets analysis

3.3.1. Turbulent kinetic energy

The collective contribution of Reynolds stresses in generating turbulent kinetic energy (TKE) is studied in this section. The transport equation for TKE is given by,

$$0 = C_k + D_k^P + D_k^T + D_k^v + P_k + \varepsilon_k \quad (6)$$

where C_k is convection term, D_k^P pressure diffusion term, D_k^T is turbulent diffusion term, D_k^v is viscous diffusion term, P_k is production term, and ε_k is dissipation term. Equation is normalized by U_{j3}^3/D . Flow axis-symmetry allows the angular gradient of mean variable to be neglected. Each term is stated as follows [Shiri, 2010]:

$$C_k = - \left\{ \overline{U} \frac{\partial k}{\partial x} + \overline{V_r} \frac{\partial k}{\partial r} - \overline{V_\theta} \frac{\overline{v_\theta'v_r'}}{r} + \overline{V_r} \frac{\overline{v_r'^2}}{r} \right\} \quad (7a)$$

$$D_k^P = - \left\{ \frac{\partial \overline{p'u'}}{\partial x} + \frac{1}{r} \frac{\partial \overline{rp'v_r'}}{\partial r} \right\} \quad (7b)$$

$$D_k^T = - \frac{1}{2} \left\{ \frac{\partial \overline{u'q^2}}{\partial x} + \frac{1}{r} \frac{\partial \overline{rv_r'q^2}}{\partial r} \right\} \quad (7c)$$

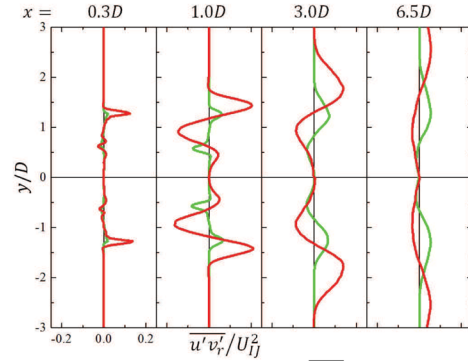


Fig. 3(e) Radial distribution of primary shear stress $\overline{u'v_r'}$. Same legend as Fig. 2(d).

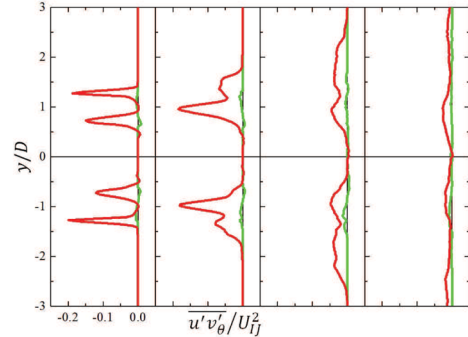


Fig. 3(f) Radial distribution of secondary shear stress $\overline{u'v_\theta'}$. Same legend as Fig. 2(d).

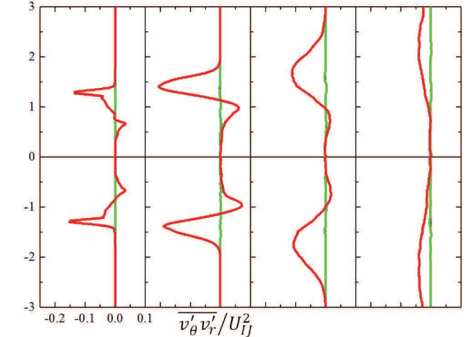


Fig. 3(g) Radial distribution of secondary shear stress $\overline{v_\theta'u'}$. Same legend as Fig. 2(d).

$$D_k^v = \frac{1}{Re_D} \left\{ \frac{\partial}{\partial x} \left(\frac{\partial k}{\partial x} + \frac{\partial \overline{u'^2}}{\partial x} + \frac{1}{r} \frac{\partial r \overline{u'v_r'}}{\partial r} \right) \right. \quad (7d)$$

$$\left. + \frac{1}{r} \frac{\partial}{\partial r} r \left(\frac{\partial k}{\partial r} + \frac{\partial \overline{u'v_r'}}{\partial x} + \frac{1}{r} \frac{\partial r \overline{v_r'^2}}{\partial r} - \frac{\overline{v_\theta'^2}}{r} \right) \right\}$$

$$P_k = -\overline{u'^2} \frac{\partial \overline{U}}{\partial x} - \overline{u'v_r'} \frac{\partial \overline{U}}{\partial r} - \overline{u'v_\theta'} \frac{\partial \overline{V_r}}{\partial x} - \overline{v_r'^2} \frac{\partial \overline{V_r}}{\partial r} - \overline{u'v_\theta'} \frac{\partial \overline{V_\theta}}{\partial x} - \overline{v_\theta'v_\theta'} \frac{\partial \overline{V_\theta}}{\partial r} \quad (7e)$$

$$\varepsilon_k = -\frac{1}{Re_D} \left\{ 2 \frac{\partial \overline{u'u'}}{\partial x} + 2 \frac{\partial \overline{v_\theta'v_\theta'}}{\partial r} - 2 \frac{\overline{v_r'^2}}{r^2} + 2 \left(\frac{1}{r} \frac{\partial \overline{v_\theta'}}{\partial \theta} \right)^2 + \left(\frac{\partial \overline{v_r'}}{\partial x} + \frac{\partial \overline{u'}}{\partial r} \right)^2 \right. \quad (7f)$$

$$\left. + \left(\frac{1}{r} \frac{\partial \overline{v_r'}}{\partial \theta} + r \frac{\partial}{\partial r} \left(\frac{\overline{v_\theta'}}{r} \right) \right)^2 + \left(\frac{\partial \overline{v_\theta'}}{\partial x} + \frac{1}{r} \frac{\partial \overline{u'}}{\partial \theta} \right)^2 \right\}$$

Fig. 4 shows the budget of TKE for the both cases at streamwise locations $x/D = 0.3, 1.0,$ and 3.0 . At $x = 0.3D$, TKE budgets exhibit insignificant activity in the jet central regions of both cases Sw0 ($r/D \leq 0.5$ for inner jet and $0.7 \leq r/D \leq 1.0$ for outer jet) and Sw18 ($r/D \leq 0.5$ for inner jet and $0.9 \leq r/D \leq 1.1$ for outer jet). Both the cases see the significant convection with negative contribution and the production of energy, whereas diffusion and dissipation also take part in a lesser extent. Note that the magnitudes of production peaks in the swirling case are

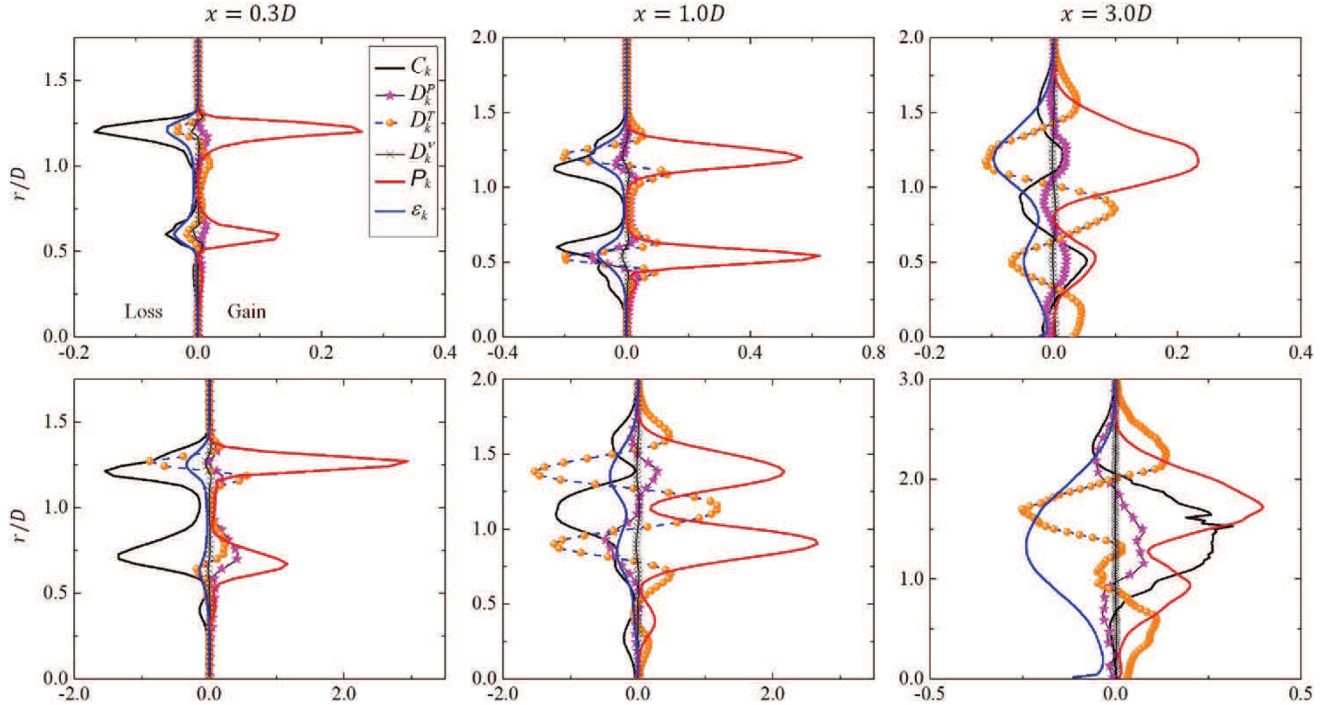


Fig. 4. Turbulent kinetic energy budget at locations $x/D = 0.3, 1.0,$ and 3.0 . Upper row: case Sw0. Lower row: case Sw18. Note that the radial extents of the distributions are changed with the downstream locations to best represent the results.

approximately 15 time higher than that in the non-swirling case. At the downstream location $x = 1.0D$, the upstream trend continues for the case Sw0 with increased contribution from the turbulent diffusion and dissipation terms. However, the central regions of both jets ($r/D \leq 0.25$ for inner jet and $0.7 \leq r/D \leq 1.0$ for outer jet) continue to show negligible values. For case Sw18, apart from the significantly higher production of TKE, a noteworthy turbulent diffusion is observed. Here, TKE produced in the regions $0.8 \leq r/D \leq 1.0$ and $1.3 \leq r/D \leq 1.5$ is transported in the outer jet central region ($1.0 \leq r/D \leq 1.3$) due to the turbulent diffusion, and hence the corresponding region sees a significant TKE (see Fig. 3(d)). The convection term is remained to be negative in both the cases and sizable pressure diffusion and dissipation are also observed. At location $x/D = 3.0$, the budgets are expanded radially with the reduced order of magnitude. Diffusion of the energy from shear layers ($0.3 \leq r/D \leq 0.7$ and $1.0 \leq r/D \leq 1.4$) to the outer jet central region ($0.7 \leq r/D \leq 1.0$) in case Sw0, which was seen at the upstream location $x = 1.0D$ in case Sw18, is taken place here. The inner jet region ($r/D \leq 0.3$) of case Sw0 and the central region ($r/D \leq 0.8$) of case Sw18 see considerable positive contribution of turbulent diffusion. Unlike the upstream location, energy is gained due to the convection in the region $0.7 < r/D < 2.0$ of case Sw18, while the equivalent amount of energy is dissipated. This suggests an important feature in which the energy for $r/D > 0.5$ (not VBB region) is convected forward from the upstream highly-energetic region to this location. However, the positive contribution of the convective term is smaller in case Sw0.

Since the interesting features, such as heightened production and higher turbulent diffusion at upstream region due to the introduction of swirl, are appeared in the TKE budget, more insight can be obtained into these features by investigating the budgets of individual Reynolds normal stresses (presented in §3.3.2).

3.3.2. Reynolds normal stresses

Transport equation for Reynolds stresses is given by,

$$0 = C_{ij} + \Pi_{ij} + D_{ij}^P + D_{ij}^T + D_{ij}^V + P_{ij} + \epsilon_{ij} \quad (8)$$

where C is convection term, Π is pressure-strain correlation term, D^P is pressure diffusion term, D^T is turbulent diffusion term, D^V is viscous diffusion term, P is production term, and ϵ is dissipation term. Subscripts for the terms of equation denote the corresponding Reynolds stress component. Terms of the above equation for each Reynolds stress are

taken in the cylindrical coordinate system [Shiri, 2010; Moser and Moin, 1984]. The equations are normalized by U_{ij}^3/D . The terms in the production are designated individually to study them separately.

Terms of momentum transfer equation for Reynolds normal stress $\overline{u'^2}$,

$$C_{uu} = - \left\{ \overline{U} \frac{\partial \overline{u'^2}}{\partial x} + \overline{V}_r \frac{\partial \overline{u'^2}}{\partial r} \right\} \quad (9a)$$

$$\Pi_{uu} = 2 p' \frac{\partial \overline{u'}}{\partial x} \quad (9b)$$

$$D_{uu}^P = -2 \frac{\partial \overline{p'u'}}{\partial x} \quad (9c)$$

$$D_{uu}^T = - \frac{\partial \overline{u'^3}}{\partial x} - \frac{1}{r} \frac{\partial \overline{r u'^2 v'_r}}{\partial r} \quad (9d)$$

$$D_{uu}^V = \frac{1}{Re_D} \left\{ \frac{\partial^2 \overline{u'^2}}{\partial x^2} + \frac{1}{r} \frac{\partial}{\partial r} \left(r \frac{\partial \overline{u'^2}}{\partial r} \right) \right\} \quad (9e)$$

$$P_{uu} = -2 \overline{u'^2} \frac{\partial \overline{U}}{\partial x} - 2 \overline{u'v'_r} \frac{\partial \overline{U}}{\partial r} \quad (9f)$$

$$\epsilon_{uu} = - \frac{2}{Re_D} \left\{ \left(\frac{\partial \overline{u'}}{\partial x} \right)^2 + \left(\frac{\partial \overline{u'}}{\partial r} \right)^2 + \left(\frac{1}{r} \frac{\partial \overline{u'}}{\partial \theta} \right)^2 \right\} \quad (9g)$$

Terms of momentum transfer equation for Reynolds normal stress $\overline{v_\theta'^2}$,

$$C_{v_\theta v_\theta} = - \left\{ \overline{U} \frac{\partial \overline{v_\theta'^2}}{\partial x} + \overline{V}_r \frac{\partial \overline{v_\theta'^2}}{\partial r} + 2 \overline{V}_r \frac{v_\theta'^2}{r} \right\} \quad (10a)$$

$$\Pi_{v_\theta v_\theta} = \frac{2}{r} p' \frac{\partial \overline{v_\theta'}}{\partial \theta} \quad (10b)$$

$$D_{v_\theta v_\theta}^P = 0 \quad (10c)$$

$$D_{v_\theta v_\theta}^T = - \frac{\partial \overline{v_\theta'^3}}{\partial x} - \frac{1}{r} \frac{\partial \overline{r v_\theta' v_\theta'^2}}{\partial r} - 2 \frac{\overline{v_\theta' v_\theta'^2}}{r} \quad (10d)$$

$$D_{v_\theta v_\theta}^V = \frac{1}{Re_D} \left\{ \frac{\partial^2 \overline{v_\theta'^2}}{\partial x^2} + \frac{1}{r} \frac{\partial}{\partial r} \left(r \frac{\partial \overline{v_\theta'^2}}{\partial r} \right) - \frac{2}{r^2} (\overline{v_\theta'^2} - \overline{v_r'^2}) \right\} \quad (10e)$$

$$P_{v_\theta v_\theta} = \underbrace{-2 \overline{u' v'_\theta} \frac{\partial \overline{V}_\theta}{\partial x}}_{P_{v_\theta v_\theta}^{u'x}} - \underbrace{2 \overline{v'_r v'_\theta} \frac{\partial \overline{V}_\theta}{\partial r}}_{P_{v_\theta v_\theta}^{v'_r r}} - \underbrace{2 \overline{v'_\theta v'_\theta} \frac{\partial \overline{V}_\theta}{\partial \theta}}_{P_{v_\theta v_\theta}^{v'_\theta \theta}} \quad (10f)$$

$$\varepsilon_{v_\theta v_\theta} = -\frac{2}{Re_D} \left\{ \overline{\left(\frac{\partial v'_\theta}{\partial x} \right)^2} + \overline{\left(\frac{\partial v'_\theta}{\partial r} \right)^2} + \frac{1}{r^2} \overline{\left(\frac{\partial v'_\theta}{\partial \theta} + v'_r \right)^2} \right\} \quad (10g)$$

Terms of momentum transfer equation for Reynolds normal stress $\overline{v_r'^2}$,

$$C_{v_r v_r} = -\left\{ \overline{U} \frac{\partial \overline{v_r'^2}}{\partial x} + \overline{V}_r \frac{\partial \overline{v_r'^2}}{\partial r} - 2 \overline{V}_\theta \frac{\overline{v_r' v'_\theta}}{r} \right\} \quad (11a)$$

$$\Pi_{v_r v_r} = 2 \rho' \frac{\partial \overline{v_r'}}{\partial r} \quad (11b)$$

$$D_{v_r v_r}^p = -\frac{2}{r} \frac{\partial r \rho' v_r'}{\partial r} \quad (11c)$$

$$D_{v_r v_r}^T = -\frac{\partial \overline{u' v_r'^2}}{\partial x} - \frac{1}{r} \frac{\partial r \overline{v_r'^3}}{\partial r} + 2 \frac{\overline{v_r' v_r'^2}}{r} \quad (11d)$$

$$D_{v_r v_r}^v = \frac{1}{Re_D} \left\{ \frac{\partial^2 \overline{v_r'^2}}{\partial x^2} + \frac{1}{r} \frac{\partial}{\partial r} \left(r \frac{\partial \overline{v_r'^2}}{\partial r} \right) + \frac{2}{r^2} (\overline{v_\theta'^2} - \overline{v_r'^2}) \right\} \quad (11e)$$

$$P_{v_r v_r} = \underbrace{-2 \overline{u' v_r'} \frac{\partial \overline{V}_r}{\partial x}}_{P_{v_r v_r}^{u'r,x}} - \underbrace{2 \overline{v_r'^2} \frac{\partial \overline{V}_r}{\partial r}}_{P_{v_r v_r}^{v_r r}} + \underbrace{2 \overline{v_r' v'_\theta} \frac{\partial \overline{V}_\theta}{\partial \theta}}_{P_{v_r v_r}^{v_r \theta, \theta}} \quad (11f)$$

$$\varepsilon_{v_r v_r} = -\frac{2}{Re_D} \left\{ \overline{\left(\frac{\partial v_r'}{\partial x} \right)^2} + \overline{\left(\frac{\partial v_r'}{\partial r} \right)^2} + \frac{1}{r^2} \overline{\left(\frac{\partial v_r'}{\partial \theta} - v'_\theta \right)^2} \right\} \quad (11g)$$

The budget analysis of Reynolds normal stresses, $\overline{u'^2}$, $\overline{v_\theta'^2}$ and $\overline{v_r'^2}$ are presented in Fig. 5(a), Fig. 5(b) and Fig. 5(c) for the both cases at the downstream locations $x/D = 0.3, 1.0$ and 3.0 respectively.

At $x = 0.3D$ (see Fig. 5(a)), the budgets for case Sw18 are significantly higher in magnitude than the budgets for case Sw0. In case Sw0, the production term is only significant in $\overline{u'^2}$ budget compared to that in other Reynolds normal stresses. On the other hand, the swirling case sees the significant increase in

production for all the normal stresses. Comparing peaks of P_{uu} for the cases Sw0 and Sw18, the value in swirling case is about five times of the value in the non-swirling case. This is reflected in the radial distribution of $\overline{u'^2}$ presented in Fig. 3(a), where the streamwise component of Reynolds normal stress in case Sw18 is higher than that in case Sw0. The production $P_{v_\theta v_\theta}$ is notably high in the swirling case, which justifies larger $\overline{v_\theta'^2}$ in the region (see Fig. 3(b)). However, the production of $\overline{v_r'^2}$ in swirling case is comparatively smaller than that of other normal stress components and the region $0.5 \leq r/D \leq 0.8$ sees a distinctive negative production of $\overline{v_r'^2}$. As a consequence of this, $\overline{v_r'^2}$ profile in case Sw18 exhibits lower intensity than $\overline{u'^2}$ (see Fig.3 (a)) and $\overline{v_\theta'^2}$ (see Fig. 3(b)). The pressure-strain correlation term Π , which is responsible for the redistribution of energy among the stress components, acts as a sink for the stress $\overline{u'^2}$ and a source for $\overline{v_\theta'^2}$ and $\overline{v_r'^2}$ in both cases. However, for case Sw18, the negative production of $\overline{v_r'^2}$ is compensated by higher Π . As observed in the budgets of TKE, both cases exhibit negative convection. In both cases, the pressure diffusion and turbulent diffusion terms show their presence in all the normal stresses. The dissipation is observed to be smaller for all normal stresses of both the cases.

At the downstream location $x/D = 1.0$ (see Fig. 5(b)), the budget magnitudes are drastically changed for both the cases with the most effect being observed in case Sw18. The overall trend in the budgets of case Sw0 is similar to the upstream location, except the turbulent diffusion term which starts to become more dominant for the budgets of all normal stress components. However, the turbulent diffusion term in case Sw0 lacks in transporting the energy from the shear layers to the outer jet central region ($0.7 \leq r/D \leq 1.0$) in contrast to the case Sw18, which sees the positive contribution of the turbulent diffusion term in the outer jet central region ($1.0 \leq r/D \leq 1.3$). For case Sw18, a significant spread is observed in the budgets, thus broadening the profiles of turbulence intensities (see Fig. 3(a), Fig. 3(b), Fig. 3(c)). A greater peak is seen at around $r/D \approx 0.9$ in the profile of $\overline{u'^2}$ of case Sw18 (see Fig. 3(a)) which can be justified by the tremendously higher production in the corresponding region. The production of $\overline{v_\theta'^2}$ is negligible for case Sw0 as observed at the upstream location $x = 0.3D$ whereas its two peaks become comparable in the case Sw18 as opposed to the upstream location. The positive contribution of production $P_{v_r v_r}$ is observed in case Sw18 however, a significant negative contribution of $P_{v_r v_r}$ is observed in case Sw18 at the ISL2 ($0.6 \leq r/D \leq 1.2$). The pressure-strain rate correlation term at the OSL ($1.2 \leq r/D \leq 1.6$) of case Sw18 exhibits a noteworthy feature in which it acts as a sink for $\overline{v_r'^2}$, and the minor source for $\overline{u'^2}$ and $\overline{v_\theta'^2}$.

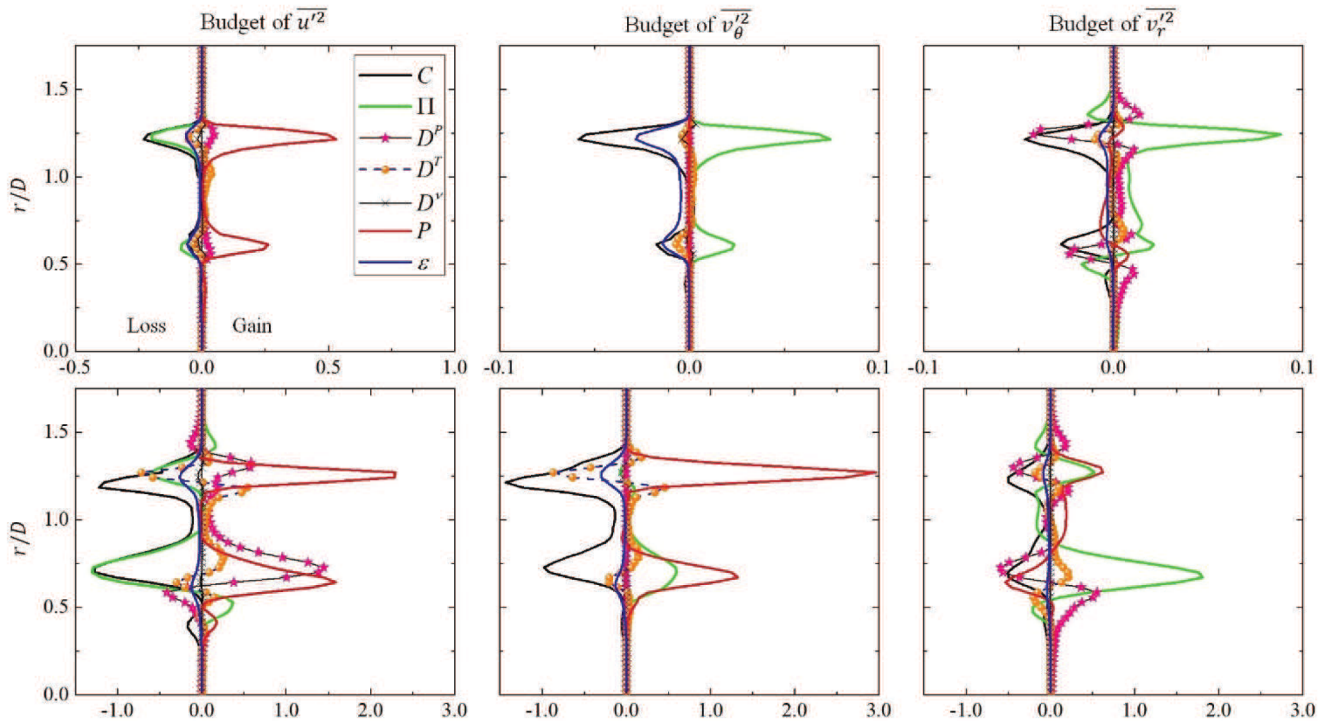


Fig. 5(a) Budgets of Reynolds normal stresses at location $x = 0.3D$. Upper row: case Sw0. Lower row: case Sw18.

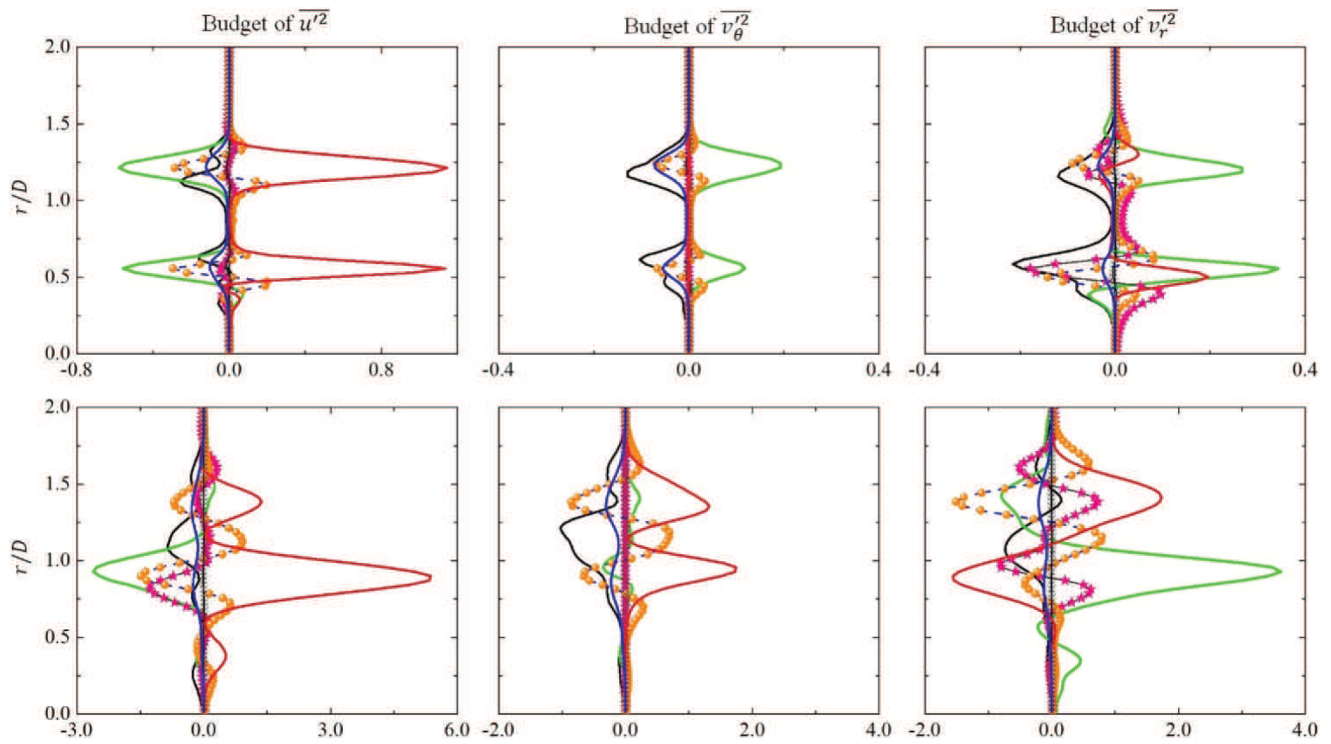


Fig. 5(b) Budgets of Reynolds normal stresses at location $x = 1.0D$. Upper row: case Sw0. Lower row: case Sw18.

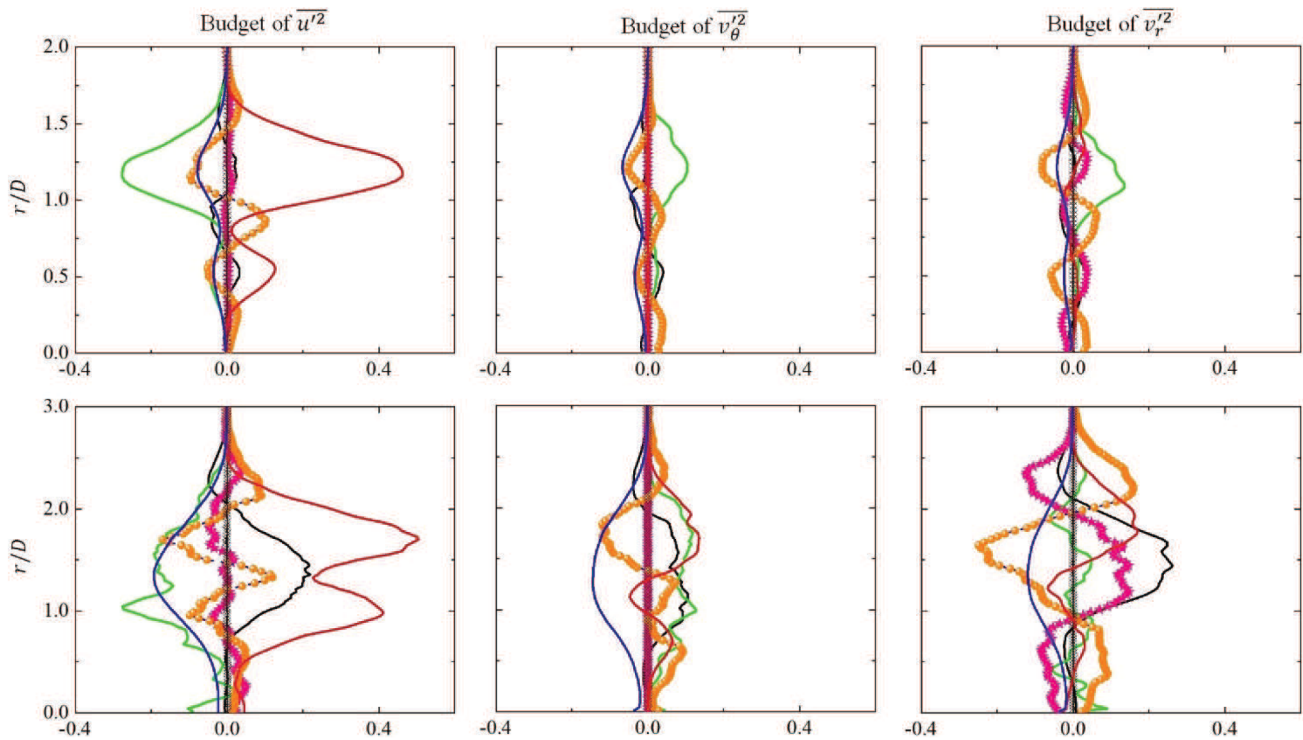


Fig. 5(c) Budgets of Reynolds normal stresses at location $x = 3.0D$. Upper row: case Sw0. Lower row: case Sw18.

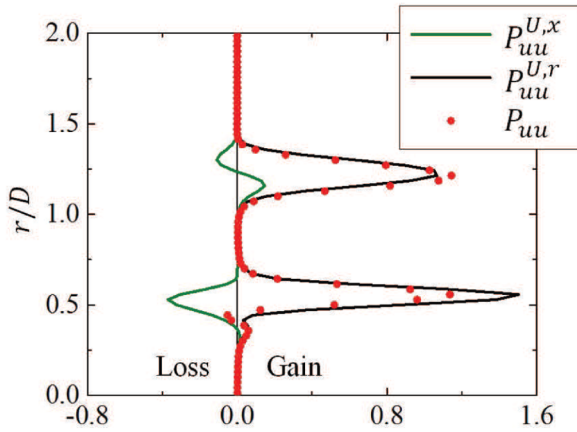


Fig. 6(a) Production terms of Reynolds stress $\overline{u^2}$ at location $x = 1.0D$ for case Sw0.

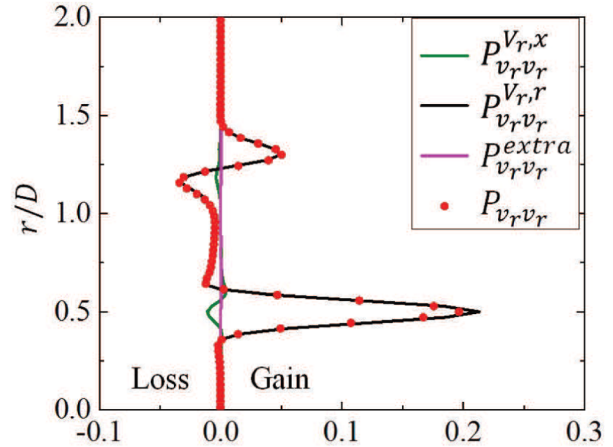


Fig. 6(d) Production terms of Reynolds stress $\overline{v_r^2}$ at location $x = 1.0D$ for case Sw0.

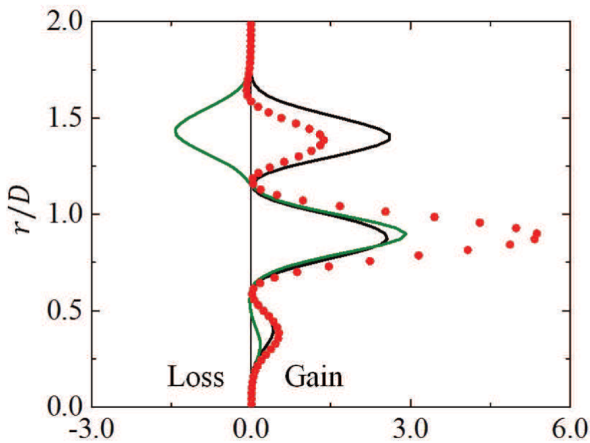


Fig. 6(b) Production terms of Reynolds stress $\overline{u^2}$ at location $x = 1.0D$ for case Sw18. Same legend as Fig. 6(a).

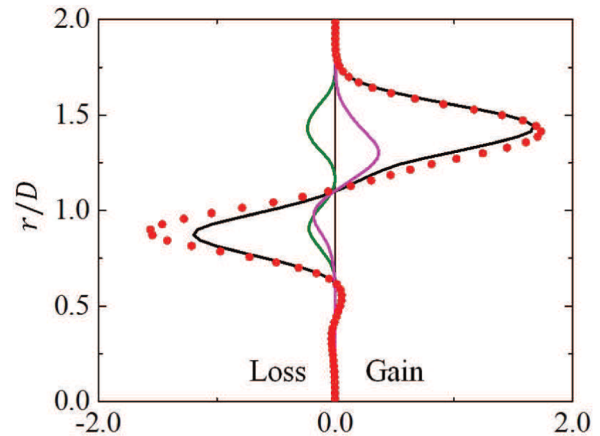


Fig. 6(e) Production terms of Reynolds stress $\overline{v_r^2}$ at location $x = 1.0D$ for case Sw18. Same legend as Fig. 6(d).

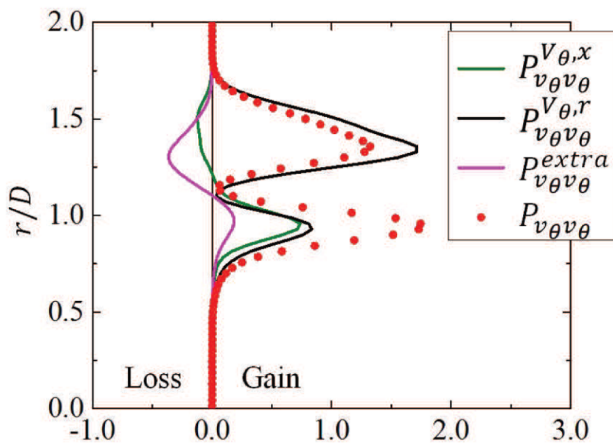


Fig. 6(c) Production terms of Reynolds stress $\overline{u_\theta^2}$ at location $x = 1.0D$ for case Sw18.

Further downstream at location $x/D = 3.0$ (see Fig. 5(c)), the order of magnitude of budgets of the case Sw18 becomes comparable to that of case Sw0. In non-swirling case, the previously equivalent two production P_{uu} peaks differ in magnitude at this location with the higher production at the OSL ($0.8 \leq r/D \leq 1.7$). This is also reflected in the distribution of the $\overline{u^2}$ where profile shows a greater peak in the same region (see Fig. 3(a)). In contrast, the previously greater peak of P_{uu} in case Sw18 at the ISL2 ($r/D \approx 1.0$) becomes equivalent to OSL peak ($r/D \approx 1.7$) and is also reflected in the distribution of $\overline{u^2}$. Negative convection witnessed at the upstream location is seen to be positive in case Sw18 and can be a reason for increasing stresses in the outer jet central region (around $r/D = 1.5$). Although the comparatively less activity is seen at the upstream locations in the central region ($r/D < 0.3$) in the budgets except for $\overline{u^2}$ and $\overline{v_r^2}$ budgets of case Sw18, the terms are observed to be non-negligible in this region at location $x = 3.0D$. The dissipation ϵ becomes one of the dominant terms at this location.

In order to investigate the cause of higher production in swirling case than the non-swirling case, the contribution of each term in the production of Reynolds normal stresses is demonstrated at the location $x/D = 1.0$. Fig. 6(a) and Fig. 6(b) demonstrates the production terms of $\overline{u^2}$ for cases Sw0 and Sw18 respectively. The term $P_{uu}^{U,r}$ is the dominant one with a positive contribution to the production in both the cases. A higher magnitude of $P_{uu}^{U,r}$ in case Sw18 is caused by the higher radial gradient of mean stream wise velocity resulted from the flow reversal between two jets (see Fig. 2(c)). The least dominant term $P_{uu}^{U,x}$ in the non-swirling case becomes larger in the swirling case. Moreover, the radial outward displacement of the outer peak of mean stream wise velocity due to the centrifugal force along with its narrowed profile results into the sign-change and inflation of $\partial \overline{u} / \partial x$ (see Fig. 2(c) and Fig. 2(d)). As a consequence, negative

contribution of the term $P_{uu}^{u,x}$ is seen at the OSL ($1.2 \leq r/D \leq 1.8$) for case Sw18, while it adds into the production at ISL2 ($0.6 \leq r/D \leq 1.2$). Fig. 6(c) demonstrates the production terms of $\overline{v_\theta^2}$ for case Sw18 only since the azimuthal momentum is negligibly small in non-swirling case resulting into the vanished $P_{v_\theta v_\theta}$. Here also the radial gradient term $P_{v_\theta v_\theta}^{v_\theta,r}$ is dominating, whereas the axial gradient term $P_{v_\theta v_\theta}^{v_\theta,x}$ is comparable to the radial gradient term at ISL2 ($0.6 \leq r/D \leq 1.2$). The extra term $P_{v_\theta v_\theta}^{extra}$ also shows its presence. Production terms of $\overline{v_r^2}$ are demonstrated in Fig. 6(d) and Fig. 6(e) for cases Sw0 and Sw18 respectively. In non-swirling case, the radial gradient term $P_{v_r v_r}^{v_r,r}$ is only seen to be contributing to the production. In swirling case, although the radial gradient term is observed to be dominant, the axial gradient term $P_{v_r v_r}^{v_r,x}$ and extra term $P_{v_r v_r}^{extra}$ also contribute to $P_{v_r v_r}$. Negative production of $\overline{v_r^2}$ observed in the ISL2 ($0.6 \leq r/D \leq 1.2$) is the result of flow divergence due to the swirling motion, which in turn results into the steep radial profiles of $\overline{v_r}$. This causes highly positive and negative radial gradients of $\overline{v_r}$ in the shear layers ISL2 ($0.6 \leq r/D \leq 1.2$) and OSL ($1.2 \leq r/D \leq 1.8$) respectively, which drive the term $P_{v_r v_r}^{v_r,r}$.

4. Conclusions

Direct numerical simulations are performed to investigate the influence of swirl on the budgets of TKE and Reynolds normal stresses for the configuration of coaxial jets, and following key observations are made:

- o Due to swirl, the turbulent diffusion term in TKE budget becomes more active in the upstream region (around $x = 1.0D$). This causes the energy level to increase in the outer jet central region of swirling case.
- o TKE in the region outside of VBB is convected from highly energetic upstream region ($x = 0.3D, 1.0D$) to the downstream region ($x = 3.0D$) in the swirling case, whereas the positive contribution by the convection term in non-swirling case seems to be smaller.
- o At $x = 1.0D$, the pressure-strain correlation term acts as energy sink for radial component of Reynolds normal stress at OSL in swirling case contrary to non-swirling case.
- o In the region upstream of central stagnation point, a distinctive negative production at ISL is observed for the radial component of normal stress in swirling case.

Acknowledgments

The simulations were carried out on Fujitsu PRIMEHPC FX100 and Fujitsu PRIMERGY CX400/270 (Information Technology Center, Nagoya University), and NEC SX-9 (Institute of Fluid Science, Tohoku University). This work was supported by JSPS KAKENHI Grant No. 18H01369. The authors express their gratitude to Dr. Kenji Tanno (Central Research Institute of Electric Power Industry, Japan) for his useful comments. The first author would like to acknowledge the financial support from Japan International Cooperation Agency.

References

- [1] Abboud, A.W., Smith, S.T., 2014. Large eddy simulation of a coaxial jet with a synthetic turbulent inlet. *International Journal of Heat and Fluid Flow* 50, 240-253.
- [2] Balaji, V.S., De, A., De, S., 2016. Numerical investigation of swirling hydrogen flames: Effect of swirl and fuel jet in coherent structures. *Journal of Energy and Environmental Sustainability* 1, 19-33.
- [3] Ben-Yeoshua, M., 1993. Coaxial jets with swirl. M.S. Thesis. The University of Arizona.
- [4] Billant, P., Chomaz, J.M., Huerre, P., 1998. Experimental study of vortex breakdown in swirling jets. *Journal of Fluid Mechanics* 376, 183-219.
- [5] Buresti, G., Petagna, P., Talamelli, A., 1998. Experimental investigation on the turbulent near-field of coaxial jets. *Experimental Thermal and Fluid Science* 17, 18-26.
- [6] Champagne, F., Kromat, S., 2000. Experiments on the formation of a recirculation zone in swirling coaxial jets. *Experiments in Fluids* 29, 494-504.
- [7] Dinesh, K.R., Kirkpatrick, M., Jenkins, K.W., 2010. Investigation of the influence of swirl on a confined coannular swirl jet. *Computers & Fluids* 39, 756-767.
- [8] Javadi, A., Nilsson, H., 2015. LES and DES of strongly swirling turbulent flow through a suddenly expanding circular pipe. *Computers & Fluids* 107, 301-313.
- [9] Kim, J., Moin, P., 1985. Application of a fractional-step method to incompressible navier-stokes equations. *Journal of Computational Physics* 59, 308-323.
- [10] Kirkpatrick, D.L., 1964. Experimental investigation of the breakdown of a vortex in a tube. Technical Report. Ministry of Aviation, Royal Aircraft Establishment.
- [11] Lucca-Negro, O., O'doherty, T., 2001. Vortex breakdown: a review. *Progress in Energy and Combustion Science* 27, 431-481.
- [12] Mehta, R., Wood, D., Clausen, P., 1991. Some effects of swirl on turbulent mixing layer development. *Physics of Fluids A: Fluid Dynamics* 3, 2716-2724.
- [13] Miyauchi, T., Tanahashi, M., Suzuki, M., 1996. Inflow and outflow boundary conditions for direct numerical simulations. *JSME International Journal Series B Fluids and Thermal Engineering* 39, 305-314.
- [14] Morinishi, Y., Lund, T.S., Vasilyev, O.V., Moin, P., 1998. Fully conservative higher order finite difference schemes for incompressible flow. *Journal of Computational Physics* 143, 90-124.
- [15] Moser, R., Moin, P., 1984. Direct numerical simulation of curved turbulent channel flow. Technical Report TM-85974. NASA.
- [16] Nocedal, J., Wright, S.J., 2006. Conjugate gradient methods. *Numerical Optimization*, 101-134.
- [17] Rehab, H., Villermaux, E., Hopfinger, E., 1997. Flow regimes of large-velocity-ratio coaxial jets. *Journal of Fluid Mechanics* 345, 357-381.
- [18] Ribeiro, M., Whitelaw, J., 1980. Coaxial jets with and without swirl. *Journal of Fluid Mechanics* 96,769-795.
- [19] Santhosh, R., Miglani, A., Basu, S., 2013. Transition and acoustic response of recirculation structures in an unconfined co-axial isothermal swirling flow. *Physics of Fluids* 25, 083603.
- [20] Sarpkaya, T., 1971. On stationary and travelling vortex breakdowns. *Journal of Fluid Mechanics* 45,545-559.
- [21] Shiri, A., 2010. Turbulence measurements in a natural convection boundary layer and a swirling jet. Ph.D. Dissertation. Chalmers University of Technology.